



Extending Counter-streaming Motion from an Active Region Filament to a Sunspot Light Bridge

Haimin Wang^{1,2} , Rui Liu³ , Qin Li^{1,2}, Chang Liu^{1,2} , Na Deng^{1,2} , Yan Xu^{1,2},
Ju Jing^{1,2}, Yuming Wang³ , and Wenda Cao²

¹ Space Weather Research Laboratory, New Jersey Institute of Technology, University Heights, Newark, NJ 07102-1982, USA; haimin.wang@njit.edu

² Big Bear Solar Observatory, New Jersey Institute of Technology, 40386 North Shore Lane, Big Bear City, CA 92314-9672, USA

³ CAS Key Laboratory of Geospace Environment, Department of Geophysics and Planetary Sciences, University of Science and Technology of China, Hefei 230026, People's Republic of China

Received 2017 November 22; revised 2017 December 13; accepted 2017 December 18; published 2018 January 4

Abstract

We analyze high-resolution observations from the 1.6 m telescope at Big Bear Solar Observatory that cover an active region filament. Counter-streaming motions are clearly observed in the filament. The northern end of the counter-streaming motions extends to a light bridge, forming a spectacular circulation pattern around a sunspot, with clockwise motion in the blue wing and counterclockwise motion in the red wing, as observed in the $H\alpha$ off-bands. The apparent speed of the flow is around $10\text{--}60\text{ km s}^{-1}$ in the filament, decreasing to $5\text{--}20\text{ km s}^{-1}$ in the light bridge. The most intriguing results are the magnetic structure and the counter-streaming motions in the light bridge. Similar to those in the filament, the magnetic fields show a dominant transverse component in the light bridge. However, the filament is located between opposed magnetic polarities, while the light bridge is between strong fields of the same polarity. We analyze the power of oscillations with the image sequences of constructed Dopplergrams, and find that the filament's counter-streaming motion is due to physical mass motion along fibrils, while the light bridge's counter-streaming motion is due to oscillation in the direction along the line-of-sight. The oscillation power peaks around 4 minutes. However, the section of the light bridge next to the filament also contains a component of the extension of the filament in combination with the oscillation, indicating that some strands of the filament are extended to and rooted in that part of the light bridge.

Key words: Sun: activity – Sun: filaments, prominences – Sun: magnetic fields

Supporting material: animations

1. Introduction

Solar filaments are cool and dense material suspended in the solar chromosphere and corona. Beyond the limb, filaments appear as bright prominences against a dark background (Tandberg-Hassen 1995). Filaments' structure and evolution are of significance in the study of solar activities, as their eruptions are closely associated with solar flares and coronal mass ejections (CMEs; Shibata & Magara 2011; Webb & Howard 2012). In particular, the two-ribbon structure of flares is often observed as filaments rise through arcade fields that subsequently reconnect. Two ribbons are associated with opposed magnetic polarities, and both run parallel to the magnetic polarity inversion line (PIL) lying between them. Such a configuration can be explained by the classical reconnection model called the CSHKP model (Carmichael 1964; Sturrock 1966; Hirayama 1974; Kopp & Pneuman 1976).

Besides the solar eruptions, filaments contain rich dynamic structure and plasma flow motions along the filament threads. The counter-streaming motion (Zirker et al. 1998) is particularly significant, and involves opposite directions of flows co-existing in filaments. Earlier investigations indicated that the counter-streaming is due to longitudinal oscillations of thin threads, restored by gravitational force (e.g., Lin et al. 2003; Karpen et al. 2006; Xia et al. 2011; Chen et al. 2014; Shen et al. 2015). Related to this, a magnetic dip is required to support the filament and balance the gravity force of the filament. We note that most prior studies targeted the quiescent filaments that are much higher than the active regions filaments. The state-of-the-art observations with high spatiotemporal resolution of the 1.6 m Goode Solar

Telescope (GST, formerly NST; Cao et al. 2010; Goode et al. 2010) at Big Bear Solar Observatory (BBSO) allows an assessment of the low atmospheric structure in unprecedented detail. As an example, Zou et al. (2016) studied GST data for an active region filament, and concluded that the filament is supported by sheared arcades and the counter-streaming motion is due to unidirectional flows with alternative directions.

Incidentally, sunspot light bridges (LBs) also received significant attention in recent years with high resolution. LBs typically have weaker yet highly inclined (Lites et al. 1991; Leka 1997) magnetic fields comparing with surrounding umbrae. Those fields are formed by large-scale convective flows (Toriumi et al. 2015a, 2015b; Felipe et al. 2016). In this regard, the fields in the LBs bear some resemblance to those of filaments, i.e., horizontal fields surrounded by the nearby more vertical fields. The difference is also very obvious: filaments are often aligned with PILs, between two sides of the opposite magnetic fields; the magnetic fields in the two sides of LBs usually have the same magnetic polarity, except those LBs dividing δ sunspots. Recently, the sunspot light walls were found to be associated with oscillation motions above LBs (e.g., Yang et al. 2015; Hou et al. 2017; Zhang et al. 2017). It would be interesting to find that chromospheric materials above LBs have counter-streaming effects that are similar to those observed in filaments.

In this Letter, we report high-resolution observations of NOAA active region (AR) 12371, on 2015 June 20, in which a filament was covered by comprehensive observations. Several sections of LBs are visible in this AR, including a section seemingly connecting to the filament. We focus on the study of

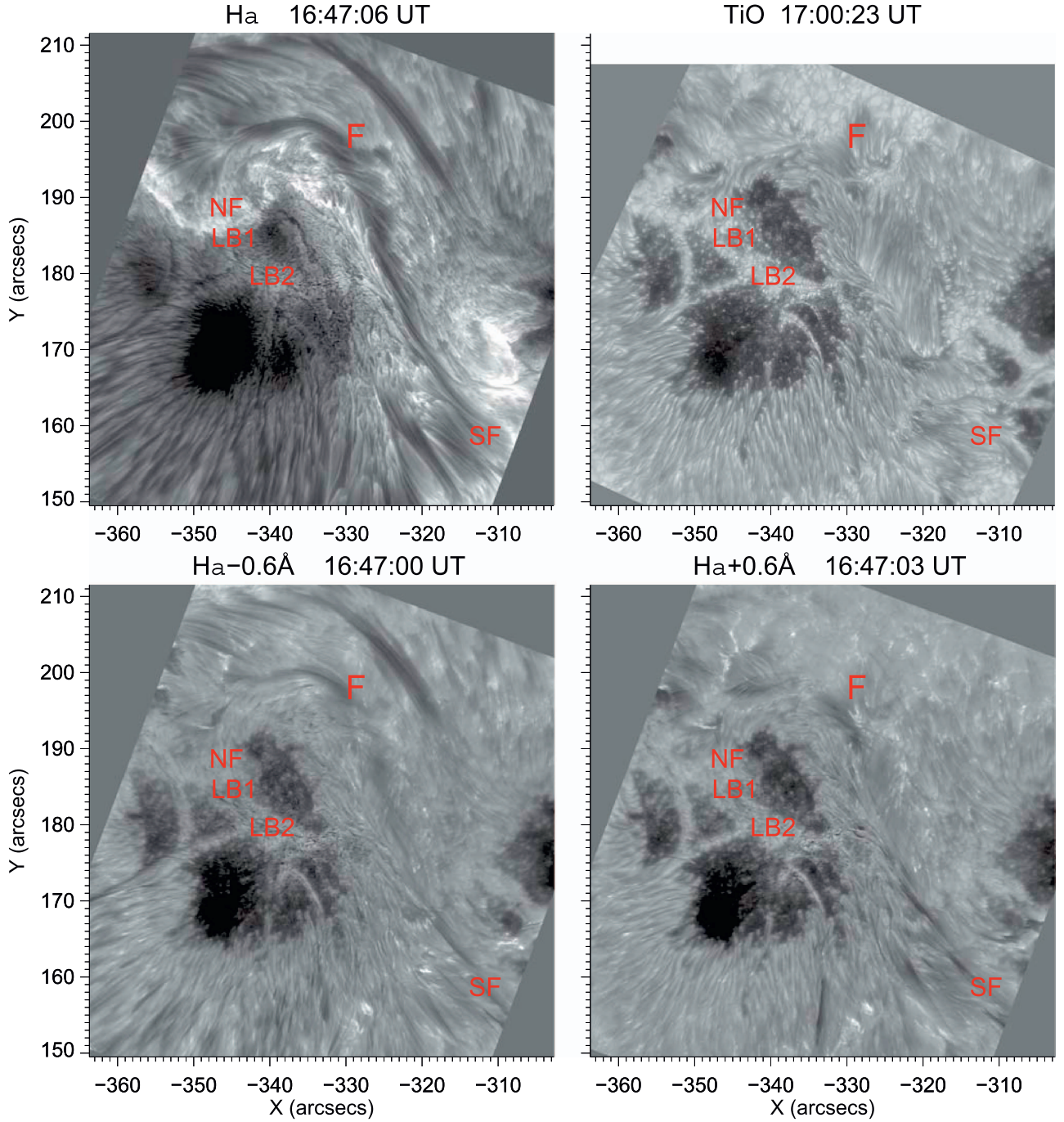


Figure 1. Top left: GST H α line center image, showing the main filament (F) and the locations of its northern footpoint (NF) and southern footpoint (SF). Top right: GST TiO image, in which three sections, i.e., LB1, LB2, and F (filament), are marked. Bottom: corresponding H α -0.6 \AA and $+0.6 \text{ \AA}$ images. The animations for the blue-wing and red-wing time sequence images show counter-streaming motions.

(Animations (a and b) of this figure are available.)

magnetic fields and flows in the filament and the connected LB. The study uses the multi-wavelength observations from GST and the *Solar Dynamic Observatory* (SDO, Pesnell et al. 2012), with the aid of the nonlinear force-free field (NLFFF) extrapolation.

2. Observations and Data Processing

With a 308-element adaptive optics system and speckle-masking image reconstruction using 100 frames, BBSO/GST

achieved diffraction-limited imaging in the TiO band (a proxy for photospheric continuum at 7057 \AA) and in H α at five wavelengths: -1.0 \AA , -0.6 \AA , line center, $+0.6 \text{ \AA}$, and $+1.0 \text{ \AA}$ on 2015 June 20. The target was the core area of NOAA AR 12371. The pixel scale of the above data sets is $0''.03$, and the cadence is nominally 30 s. The GST observations covered about six hours under excellent and consistent seeing conditions.

The full-disk vector magnetic field data with a 12-minute cadence from the Helioseismic and Magnetic Imager (HMI;

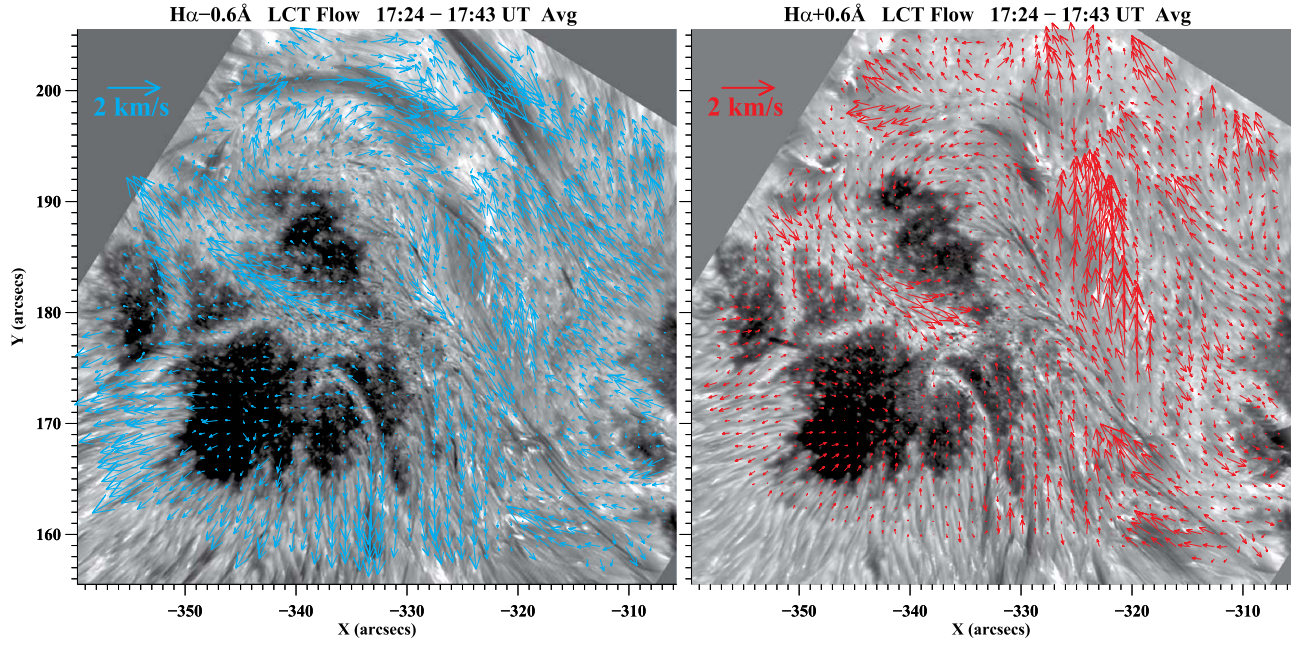


Figure 2. Flows derived using the LCT method. Left: blue-wing flow map. Right: red-wing flow map. The counter-streaming motion is apparent along F-LB1-LB2 as marked in Figure 1. The magnitude of the flow speed is averaged over static and moving components.

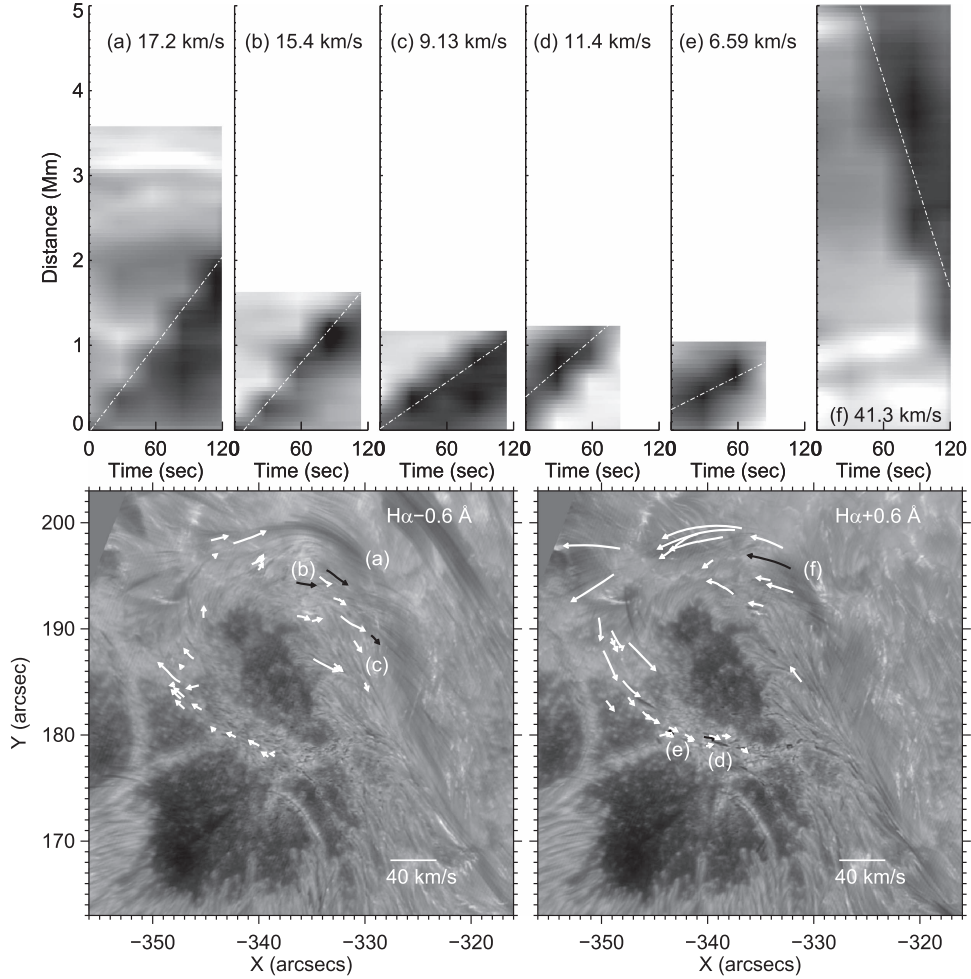


Figure 3. Top: selected examples of time-space diagrams from which the flow speeds are derived. Bottom: $H\alpha$ blue- and red-wing images at the off-band of 0.6 \AA from the $H\alpha$ line center, overplotted by flow vectors along selected $H\alpha$ fibrils. The flow is derived based on time-distance plots. Following Figure 2, counter-streaming is apparent around the sunspot, connecting F, LB1, and LB2, but the flow speed is much higher.

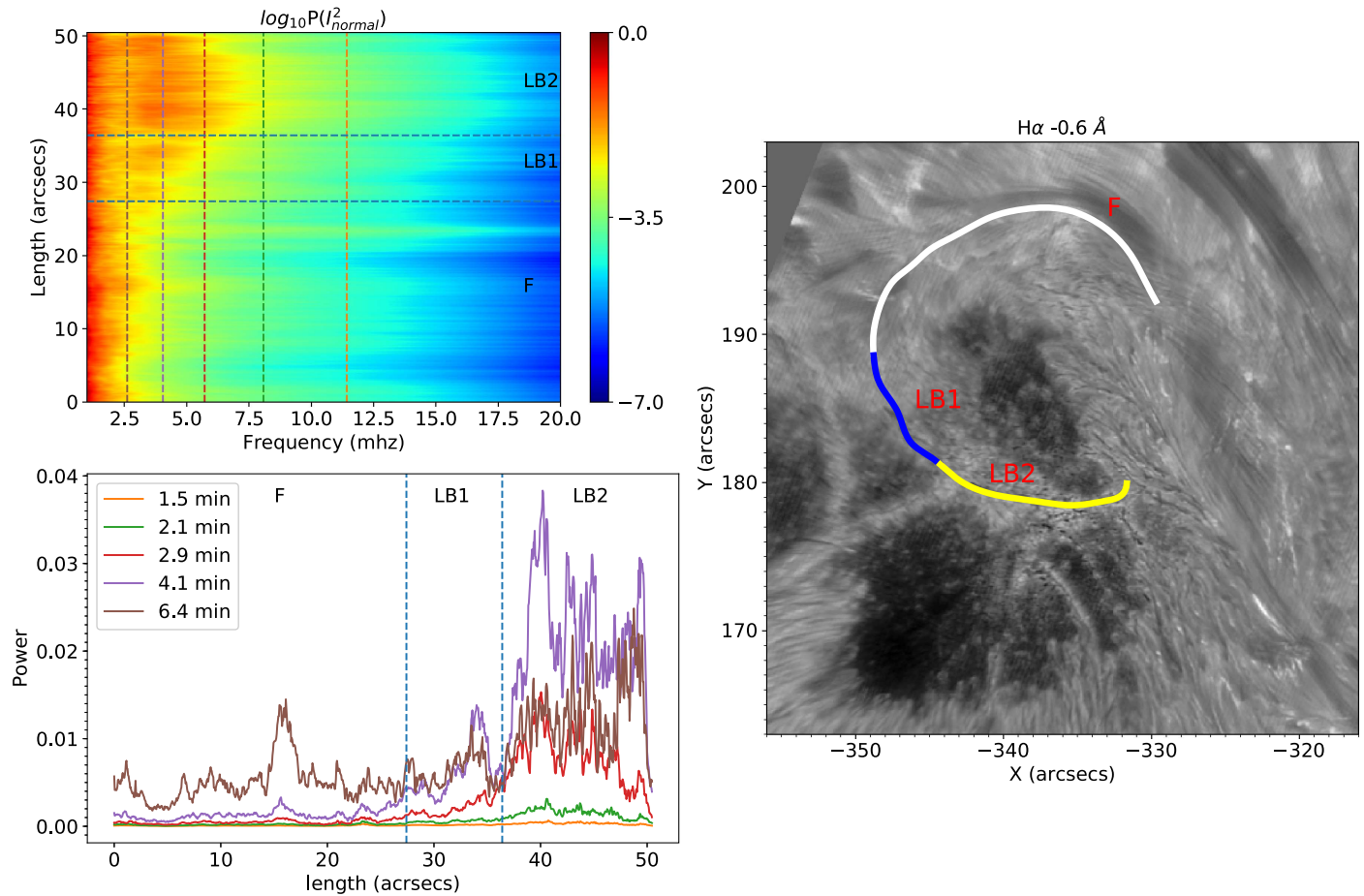


Figure 4. Top left: oscillation power along a trajectory (defined in the right panel) that connects F, LB1, and LB2. The power is derived using wavelet analysis of pseudo-Dopplergrams based on the difference between $H\alpha -0.6 \text{ \AA}$ and $H\alpha +0.6 \text{ \AA}$ images. The oscillation power in LB2 is 3 times larger than that in LB1, and more than an order of magnitude larger than the filament. This is demonstrated more clearly in the lower left panel, where the powers of several frequencies are plotted. The purple line is the oscillation power at a period of 4.1 minutes, at which the oscillation power peaks.

Schou et al. 2012) on board *SDO* are derived using the VFISV inversion code by Borrero et al. (2011). The accuracy of HMI magnetograms is 10 G for line-of-sight fields and 100 G for transverse fields. After preprocessing the photospheric boundary to best suit the force-free condition (Wiegmann et al. 2006), we constructed NLFFF models using the “weighted optimization” method (Wiegmann 2004) with the error treatment incorporated (Wiegmann & Inhester 2010; Wiegmann et al. 2012). Ancillary data in 1700 \AA from the Atmospheric Imaging Assembly (AIA; Lemen et al. 2012) on board *SDO* were also used.

The images at different wavelengths are aligned with feature matching. TiO images are easily aligned with $H\alpha$ far wings and continuum images of HMI and AIA. HMI magnetograms are then aligned with reference to the HMI continuum. The alignment accuracy is less than $1''$.

3. Results

In Figure 1, we show the context images to define different areas under study. The active region filament (marked with the letter F) is shown clearly in the $H\alpha$ line center image. Its two footpoints are marked as SF (Southern Footpoint) and NF (Northern Footpoint). Viewing larger-scale structures from full-disk $H\alpha$ images, this filament is one leg of a sigmoid structure, with the SF lying toward the center of the sigmoid. In the

corresponding TiO image, we divide the region surrounding the top sunspot into three sections, Light Bridge Section 1 (LB1), Light Bridge Section 2 (LB2), and a penumbral region corresponding to the filament (F) in $H\alpha$. In the bottom part of the figure we show $H\alpha -0.6 \text{ \AA}$ and $+0.6 \text{ \AA}$ images. The flow motions under study are most obvious in these wavelengths. The accompanied movies of $H\alpha -0.6 \text{ \AA}$ and $+0.6 \text{ \AA}$ demonstrate the circular counter-streaming motions spanning from the filament to the LB (LB1 and LB2). Animation (a) shows clockwise motion, while animation (b) shows counterclockwise motion.

We use two methods to measure the speed of the flow motion. Figure 2 shows the results of local correlation tracking (LCT). Although in general the motion direction matches with visual inspection of the movies, the derived magnitude of the counter-streaming motion in the order of 1 km s^{-1} is substantially underestimated. The reason is that the flow motions only exist along certain fibrils, while the LCT gives an average flow speed. Therefore, we use the time-slice method to manually measure the flow speed along certain prominent fibrils (see Li et al. 2017). Figure 3 shows the results. Based on the measurements of about 100 moving features, the flow speed is $20\text{--}60 \text{ km s}^{-1}$ in this section of the filament and is reduced to $5\text{--}20 \text{ km s}^{-1}$ in the LB. The moving fibrils are substantially longer in the filament (as long as $30''$, compared to $1''\text{--}3''$ in the LB). The speed in the red wing is higher than that in the blue

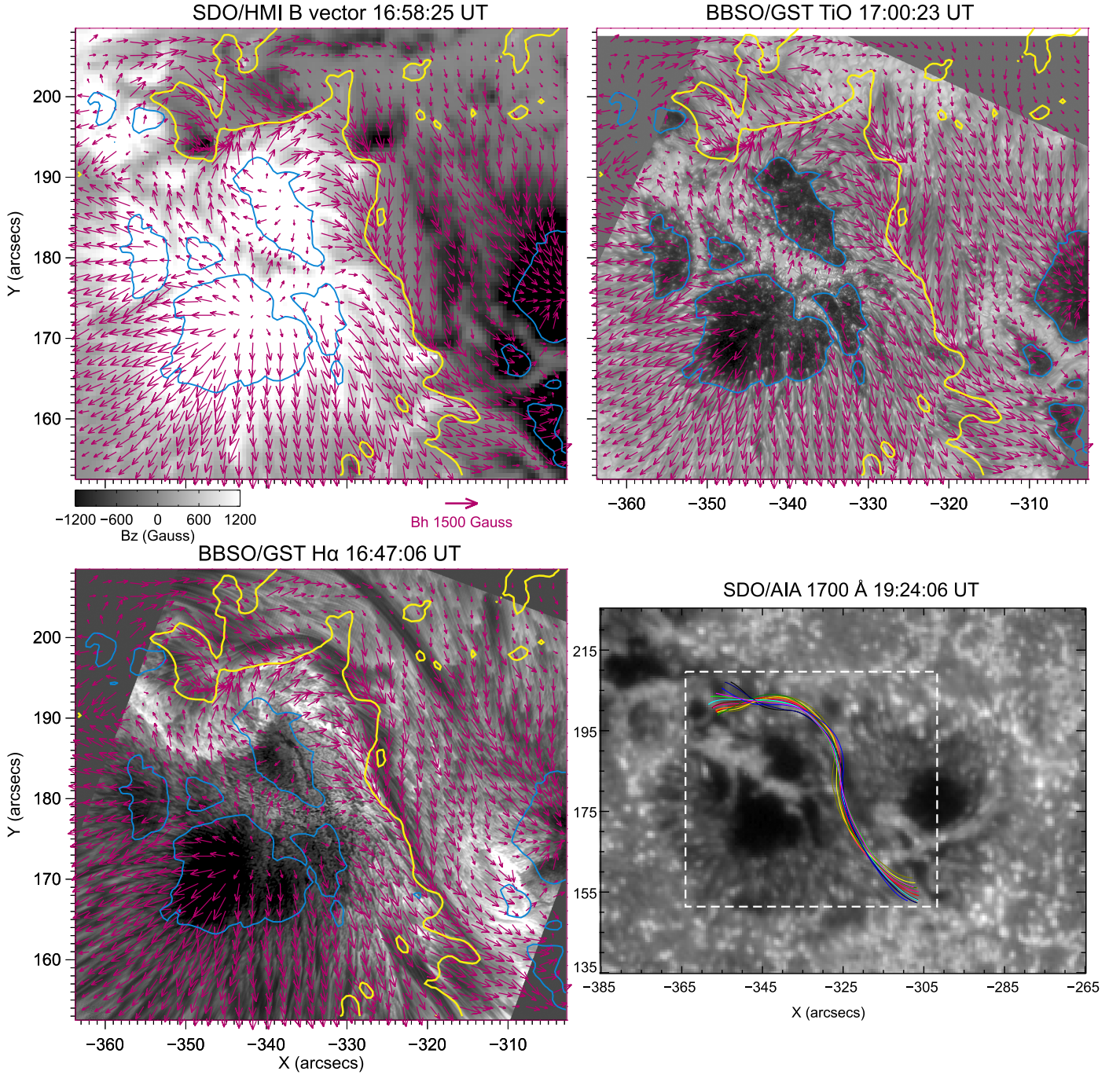


Figure 5. Top left: HMI vector magnetic field plot. Top right and bottom left: transverse field overplotted on TiO and H α line center images, showing the clockwise circulation of field lines extending from the filament to LB. The blue contours mark the borders of umbrae, while the yellow contours mark the PIL. Bottom right: flux rope derived from NLFFF extrapolation, overplotted on an AIA 1700 Å image. The dashed box shows the FOV of the other three panels.

wing in the filament (40 versus 20 km s⁻¹) and LB1 (20 versus 10 km s⁻¹). In LB2, the mean speed is about 5 km s⁻¹ for both wings.

To determine if the observed flow motion is a mass motion or a signature of chromospheric oscillations of filament threads, we construct pseudo-Dopplergrams using the difference between the red-wing and blue-wing images of ± 0.6 Å. Wavelet analysis is then performed on the time sequence of Dopplergrams to derive the power of possible periodic motions. The wavelet power spectra are calculated using the Morlet wavelet analysis technique of Torrence & Compo

(1998), which provides excellent time and frequency localization information. In general, throughout the AR, the oscillation power peaks at the period around 4 minutes (4.2 mHz), which is between the photospheric p -mode and 3-minute chromospheric oscillation. In Figure 4, we plot the power of oscillation along a curve connecting F, LB1, and LB2. The mean 4-minute oscillating powers are 0.0014, 0.0063, and 0.021 in F, LB1, and LB2, respectively. It is obvious that in the filament, the oscillation power is at least one order of magnitude smaller than that in LB2. Therefore, we conclude that the mass flow is the mechanism for the counter-streaming motion in the

filament, while the oscillation is the likely cause of the apparent counter-streaming motion in LB2. Notably, LB1 is an interesting section. It shows short, hairy, and somewhat Y-shaped patterns; meanwhile, some strands of the filament also extend to this section with substantially longer fibrils (in the size of about 2000–3000 km, in comparison to a typical background size of 700 km in both LB1 and LB2). It has a dominant component of oscillation with a period of 4–6 minutes, therefore the underlying physical mechanism is similar to that in LB2. However, compared to LB2 the oscillation power in LB1 is reduced by a factor of 3. We conclude that LB1 has a hybrid nature, as it combines the characteristics of oscillation motion and the mass motion extended from the filament.

The next step is to analyze the magnetic topology around the sunspot, including the filament and the LB. Figure 5 shows the vector magnetic field plot with the HMI data, which demonstrates a clockwise circulation pattern of transverse field vectors from LB2 to LB1 and to F. The lower right panel of Figure 5 shows the result of NLFFF extrapolation that resembles the filament well. The southern endpoint is well defined and matches with the tracing in $H\alpha$. The northern end of the filament does not match the $H\alpha$ tracing well. We believe that the NLFFF extrapolation emphasizes magnetic connectivity at higher altitudes where the NLFFF conditions are better satisfied, while the $H\alpha$ observation shows the lower atmospheric structure. Therefore, the trajectory of continuous motion in the chromosphere is not reflected in the traced NLFFF flux rope from the filament to LB1. On the other hand, the $H\alpha$ material might trace only certain segments of field lines.

4. Summary and Discussion

We have presented a detailed study of flows and magnetic fields around a sunspot in AR 12371. Here are the key results.



1. This is the first time that counter-streaming motions circulating around a sunspot are observed. In the $H\alpha$ blue wing the motion appears to be clockwise, and in the red wing, it appears to be counterclockwise.
2. In LB2 it shows a prominent signature of oscillations. The maximum power is at the period around 4 minutes. In LB1, the dominant motion is similar to that in LB2. However, the power is reduced by a factor of 3. In the meantime, some filament strands extend to LB1, thus the resulting component of the counter-streaming motion is due to the physical mass motion along fibrils, resembling that in the filament. It is possible that the oscillation is related to the surge-like oscillation above LBs, as shown by Yang et al. (2015), Zhang et al. (2017), and Hou et al. (2017) using IRIS data. However, the LB under this study is much wider than those studied in the above papers. As the observed motion is toward the solar limb (disk center) in the blue-wing (red-wing) images, the oscillation has to be perpendicular to the solar surface.
3. The magnetic field circulates around the sunspot in the clockwise direction, connecting the LB and the filament.
4. The flux rope identified in the NLFF field shows consistency in the southern footpoint and the spiral orientation compared to the $H\alpha$ filament. The northern footpoint is slightly mismatched.

Based on the above observational results, the observed counter-streaming motion in LB1 and LB2 is likely due to

oscillation perpendicular to the solar surface. The mass flows in the filament are likely due to pressure imbalance, as discussed in previous articles (e.g., Zou et al. 2016). It is likely that the horizontal fields of part of the filament extend to LB1, as evidenced by an additional component of counter-streaming motions of longer fibrils in LB1. Consequently, some branches of the northern end of the filament are anchored in the LB1. This mixture of oscillation and physical mass flows reduces the oscillation power in LB1. Our study could not identify a one-to-one relationship between footpoint disturbances and the associated mass flows in episodes of counter-streaming flows in the filament. The apparent circular counter-streaming motion is thus due to the combination of all the above effects.

We are grateful to the referee for the very helpful comments that improved the Letter. We acknowledge the BBSO and SDO teams for providing the data. This work is supported by NSF under grants AGS 1348513, 1408703, and 1539791. R. Liu acknowledges NSFC 41474151 and 41774150 grants. H.W. acknowledges the International Visiting Professor Program of USTC.

ORCID iDs

Haimin Wang  <https://orcid.org/0000-0002-5233-565X>
 Rui Liu  <https://orcid.org/0000-0003-4618-4979>
 Chang Liu  <https://orcid.org/0000-0002-6178-7471>
 Na Deng  <https://orcid.org/0000-0001-8179-812X>
 Yuming Wang  <https://orcid.org/0000-0002-8887-3919>

References

- Borrero, J. M., Tomczyk, S., Kubo, M., et al. 2011, *SoPh*, **273**, 267
 Cao, W., Gorceix, N., Coulter, R., et al. 2010, *AN*, **331**, 636
 Carmichael, H. 1964, in *The Physics of Solar Flares*, ed. W. N. Hess (Washington, DC: NASA), 451
 Chen, P. F., Harra, L. K., & Fang, C. 2014, *ApJ*, **784**, 50
 Felipe, T., Collados, M., Khomenko, E., et al. 2016, *A&A*, **596**, 59
 Goode, P. R., Yurchyshyn, V., Cao, W., et al. 2010, *ApJL*, **714**, L31
 Hirayama, T. 1974, *SoPh*, **34**, 323
 Hou, Y., Zhang, J., Li, T., Yang, S., & Li, X. 2017, *ApJL*, **848**, L9
 Karpen, J. T., Antiochos, S. K., & Klimchuk, J. A. 2006, *ApJ*, **637**, 531
 Kopp, R. A., & Pneuman, G. W. 1976, *SoPh*, **50**, 85
 Leka, K. D. 1997, *ApJ*, **484**, 900
 Lemen, J. R., Title, A. M., Akin, D. J., et al. 2012, *SoPh*, **275**, 17
 Li, Q., Deng, N., Jing, J., & Wang, H. 2017, *ApJ*, **841**, 112
 Lin, Y., Engvold, O. R., & Wilk, J. E. 2003, *SoPh*, **216**, 109
 Lites, B. W., Bida, T. A., Johannesson, A., & Scharmer, G. B. 1991, *ApJ*, **373**, 683
 Pesnell, W. D., Thompson, B. J., & Chamberlin, P. C. 2012, *SoPh*, **275**, 3
 Schou, J., Scherrer, P. H., Bush, R. I., et al. 2012, *SoPh*, **275**, 229
 Shen, Y., Liu, Y., Liu, Y. D., et al. 2015, *ApJ*, **814**, 17
 Shibata, K., & Magara, T. 2011, *LVSP*, **8**, 6
 Sturrock, P. A. 1966, *Natur*, **211**, 695
 Tandberg-Hassen, E. 1995, *The Nature of Solar Prominences* (Dordrecht: Kluwer), 199
 Toriumi, S., Cheung, M. C., & Katsukawa, Y. 2015a, *ApJ*, **811**, 138
 Toriumi, S., Katsukawa, Y., & Cheung, M. C. 2015b, *ApJ*, **811**, 137
 Torrence, C., & Compo, G. P. 1998, *BAMS*, **79**, 61
 Webb, D. F., & Howard, T. A. 2012, *LVSP*, **9**, 3
 Wiegmann, T. 2004, *SoPh*, **219**, 87
 Wiegmann, T., & Inhester, B. 2010, *A&A*, **516**, A107
 Wiegmann, T., Inhester, B., & Sakurai, T. 2006, *SoPh*, **233**, 215
 Wiegmann, T., Thalmann, J. K., Inhester, B., et al. 2012, *SoPh*, **281**, 37
 Xia, C., Chen, P. F., Keppens, R., & van Marle, A. J. 2011, *ApJ*, **737**, 27
 Yang, S., Zhang, J., Jiang, F., & Xiang, Y. 2015, *ApJL*, **804**, L27
 Zhang, J., Tian, H., He, J., & Wang, L. 2017, *ApJ*, **838**, 2
 Zirker, J. B., Engvold, O., & Matin, S. F. 1998, *Natur*, **396**, 440
 Zou, P., Fang, C., Chen, P. F., et al. 2016, *ApJ*, **831**, 123